Graphene disk in a solenoid magnetic potential: Aharonov-Bohm effect without a two-slit-like setup

Adam Rycerz and Dominik Suszalski
Institute for Theoretical Physics, Jagiellonian University, Łojasiewicza 11, PL–30348 Kraków, Poland

(Received 8 April 2020; revised manuscript received 29 May 2020; accepted 2 June 2020; published 22 June 2020)

The Aharonov-Bohm effect allows one to demonstrate the physical meaningfulness of magnetic vector potential bypassing the current in zero magnetic field regions. In the standard (a *two-slit-like*) setup, a conducting ring is pierced by magnetic flux and the quantum interference for an electron passing simultaneously through the two ring arms is observed. Here we show, by analyzing transport via evanescent waves, that the ballistic Corbino disk in graphene subjected to a solenoid magnetic potential may exhibit conductance oscillations of the Aharonov-Bohm kind although the current flows through a single conducting element only.

DOI: 10.1103/PhysRevB.101.245429

I. INTRODUCTION

Quantum transport through the Corbino disk in graphene has been addressed both theoretically [1–7] and experimentally [8–12] by numerous authors, as the egde-free geometry allows one to probe the mesoscopic aspects of graphene, such as transport via evanescent waves [13], even in nanometer-scale devices. At zero magnetic field, conductance of ultra-clean ballistic disks as a fuction of the carrier concentration [10] shows good agreement with the basic mode-matching analysis of Ref. [1]. At nonzero field, periodic (approximately sinusoidal) magnetoconductance oscillations were predicted [2,3] but experimental confirmation of such a remarkable quantum-interference phenomenon is missing.

Theoretical analysis of Ref. [2] employs the rotational symmetry of the problem, resulting in the total angular momentum conservation ($J_z = \hbar j$, with $j = \pm 1/2, \pm 3/2, \ldots$, the angular-momentum quantum number). In the case of an undoped disk of the inner radius R_1 and the outer radius R_2, the Landauer-Büttiker transmission probabilities [14,15] read

$$T_j = \frac{1}{\cosh^2[\ln(R_2/R_1)(j + \Phi_d/\Phi_0)]}, \tag{1}$$

where $\Phi_d = \pi(R_2^2 - R_1^2)B$ is the flux piercing the disk with a uniform magnetic field B, and $\Phi_0 = 2(h/e)\ln(R_2/R_1)$ defines the conductance-oscillation period. Further analysis shows that the formula equivalent to Eq. (1) can also be derived if the carrier concentration (hereinafter quantified by the Fermi energy E_F, with $E_F = 0$ corresponding to the charge-neutrality point) is adjusted to any Landau level, $E_n = \mathrm{sgn}(n) v_F \sqrt{2|n|e\hbar B}$, with $n = 0, \pm 1, \pm 2, \ldots$, and $v_F \approx 10^6$ m/s being the energy-independent Fermi velocity in graphene.

Away from Landau levels the transmission is strongly suppressed [2,7]. For instance, in the vicinity of the charge-neutrality point ($n = 0$) magnetoconductance oscillations may be observed in the magnetic field range limited by

$$|\Phi_d| \lesssim \frac{2h}{e} \ln\left(\frac{1}{k_F R_1}\right) = \frac{h}{e} \ln\left(\frac{1}{\pi |n_C| R_1^2}\right), \tag{2}$$

where we have further defined $k_F = |E_F|/(\hbar v_F)$ and the outermost right equality follows from the relation between the Fermi wave number and the carrier concentration (n_C), namely, $k_F = \sqrt{\pi |n_C|}$, including the fourfold (spin and valley) degeneracy of each quasiparticle level. On the other hand, the current flow through the system leads to carrier density fluctuations of the order of $\delta n_C \sim 1/(\pi R_2{}^2)$, even in the absence of the charge inhomogeneity usually appearing due to the electron-hole puddle formation at low densities [16]. Taking the above as the lower bound to $|n_C|$ in Eq. (2), one immediately obtains $|\Phi_d| \lesssim \Phi_0$, suggesting it may be difficult (or even impossible) to observe the magnetoconductance oscillations in the linear-response regime. A proposal to overcome this difficulty by going beyond the linear-response regime was put forward [17].

A separate issue concerns the role of electron-electron interactions, which is usually marginal when discussing ballistic systems in monolayer graphene [18,19], in agreement with fundamental considerations [20,21], but may lead to Wigner crystallization or the appearance of fractional quantum Hall phases, in case the bulk density of states is strongly modified due to the Landau quantization [10,22,23].

Generally speaking, uniform magnetic fields, although being most feasible to generate at micrometer scale, do not seem to provide a realistic opportunity to observe magnetoconductance oscillations in graphene-based Corbino disks. Therefore it is worth to consider other field arrangemets, in which phase effects may overrule orbital effects (such as Landau level formation). In this paper, we focus on the case of a disk whose inner area is pierced by a long solenoid (see Fig. 1), generating the flux Φ_i. Earlier, it was shown by Katsnelson [3,24] that for zero doping ($E_F = 0$) the transmission probabilities are given

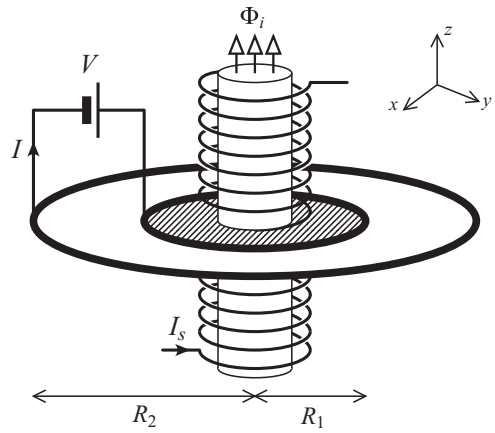

FIG. 1. Schematic of the Corbino disk in graphene of the inner radius R_1 and the outer radius R_2, contacted by two electrodes (thick black circles). A voltage source (V) drives the current (I) through the disk. A separate gate electrode (not shown) allows the carrier concentration in the disk to be tuned around the neutrality point. A long solenoid, carrying the current I_s, generates the flux Φ_i piercing the inner disk area. The coordinate system is also shown.

by Eq. (1) after substituting

$$\Phi_d \equiv \Phi_i \quad \text{and} \quad \Phi_0 \equiv \Phi_{\mathrm{AB}}, \tag{3}$$

with $\Phi_{\mathrm{AB}} = h/e$ being the familiar Aharonov-Bohm flux quantum [25]. However, the analysis of such a system away from the charge-neutrality point ($E_F \neq 0$) is missing.

The remaining part of the paper is organized as follows. In Sec. II, we present the results of the mode-matching analysis for the system of Fig. 1 at arbitrary doping and flux. Next, in Sec. III, the numerical discussion of the conductance oscillations is provided. The effect of electrostatic field breaking cylindrical symmetry of the problem is considered in Sec. IV. The conclusions are given in Sec. V.

II. SOLUTION FOR ARBITRARY DOPING AND FLUX

Our analysis starts from the Dirac Hamiltonian in a single valley (K), which is given by

$$H = v_F(\boldsymbol{p} + e\boldsymbol{A})\cdot\boldsymbol{\sigma} + U(r), \tag{4}$$

where $\boldsymbol{p} = -i\hbar(\partial_x, \partial_y)$ is the in-plane momentum operator, the electron charge is $-e$, the magnetic vector potential of a solenoid is written in the symmetric gauge [26]

$$\boldsymbol{A} = (A_x, A_y) = \frac{\Phi_i}{2\pi}\left(-\frac{y}{r^2}, \frac{x}{r^2}\right), \tag{5}$$

and $\boldsymbol{\sigma} = (\sigma_x, \sigma_y)$ with σ_x and σ_y being the Pauli matrices. We further suppose that the electrostatic potential energy $U(r)$ depends only on $r = \sqrt{x^2 + y^2}$; namely, we put $U(r) = 0$ in the disk area ($R_1 < r < R_2$), or $U(r) = U_\infty$ otherwise. Since Hamiltonian (4) commutes with the total angular momentum operator, $J_z = -i\hbar\partial_\varphi + \hbar\sigma_z/2$, the energy eigenfunctions can be chosen as eigenstates of J_z

$$\psi_j(r,\varphi) = e^{i(j-1/2)\varphi}\begin{pmatrix}\chi_{j,A}(r)\\ \chi_{j,B}(r)e^{i\varphi}\end{pmatrix}, \tag{6}$$

where j is a half-odd integer, two spinor components (A, B) correspond to the sublattice degree of freedom, and we have introduced the polar coordinates (r, φ). The Dirac equation now can be written as $H_j(r)\chi_j(r) = E\chi_j(r)$, where $\chi_j(r) = [\chi_{j,A}(r), \chi_{j,B}(r)]^T$, and

$$H_j(r) = -i\hbar v_F\sigma_x\partial_r + U(r) + \hbar v_F\sigma_y\begin{pmatrix}\frac{j-1/2}{r} + \frac{e\Phi_i}{\hbar r} & 0\\ 0 & \frac{j+1/2}{r} + \frac{e\Phi_i}{\hbar r}\end{pmatrix}. \tag{7}$$

For a piecewise-constant potential energy $U(r)$ and the electron-doping case, $E > U(r)$, the eigenfunctions of $H_j(r)$ (7) for the incoming (i.e., propagating from $r = 0$) and outgoing (propagating from $r = \infty$) waves are given, up to the normalization, by

$$\chi_j^{\mathrm{in}} = \begin{pmatrix}H^{(2)}_{\nu(j)-1/2}(kr)\\ iH^{(2)}_{\nu(j)+1/2}(kr)\end{pmatrix}, \quad \chi_j^{\mathrm{out}} = \begin{pmatrix}H^{(1)}_{\nu(j)-1/2}(kr)\\ iH^{(1)}_{\nu(j)+1/2}(kr)\end{pmatrix}, \tag{8}$$

where

$$\nu(j) = j + \Phi_i/\Phi_{\mathrm{AB}}, \tag{9}$$

$H_\nu^{(1,2)}(\rho)$ is the Hankel function of the (first, second) kind, and $k = |E - U(r)|/(\hbar v_F)$. The solution for the disk area can be represented as

$$\chi_j^{(d)} = A_j\chi_j^{\mathrm{in}}(k_F r) + B_j\chi_j^{\mathrm{out}}(k_F r), \quad R_1 < r < R_2, \tag{10}$$

with A_j and B_j being arbitrary constants, and the Fermi wave number $k_F = |E|/(\hbar v_F)$. For the hole doping case, $E < U(r)$, the wave functions are replaced by $\tilde{\chi}_j^{\mathrm{in(out)}} = [\chi_j^{\mathrm{in(out)}}]^\star$, where we use the relation $H_\nu^{(2)} = [H_\nu^{(1)}]^\star$.

The heavily doped graphene leads are modeled here by taking the limit of $U(r) = U_\infty \to \pm\infty$ for $r < R_1$ or $r > R_2$. The corresponding wave functions can be simplified to

$$\chi_j^{(1)} = \frac{e^{\pm ik_\infty}}{\sqrt{r}}\begin{pmatrix}1\\1\end{pmatrix} + r_j\frac{e^{\mp ik_\infty}}{\sqrt{r}}\begin{pmatrix}1\\-1\end{pmatrix}, \quad r < R_1, \tag{11}$$

$$\chi_j^{(2)} = t_j\frac{e^{\pm ik_\infty}}{\sqrt{r}}\begin{pmatrix}1\\1\end{pmatrix}, \quad r > R_2, \tag{12}$$

where we have introduced the reflection (transmission) amplitudes r_j (t_j) and $k_\infty = |E - U_\infty|/(\hbar v_F) \to \infty$.

Solving the mode-matching conditions, $\chi_j^{(1)}(R_1) = \chi_j^{(d)}(R_1)$ and $\chi_j^{(d)}(R_2) = \chi_j^{(2)}(R_2)$, we find the transmission probability for jth mode

$$T_j = |t_j|^2 = \frac{16}{\pi^2k^2R_1R_2}\frac{1}{\left[\mathfrak{D}^{(+)}_{\nu(j)}\right]^2 + \left[\mathfrak{D}^{(-)}_{\nu(j)}\right]^2}, \tag{13}$$

where $\nu(j)$ is given by Eq. (9) and

$$\mathfrak{D}^{(\pm)}_\nu = \mathrm{Im}\big[H^{(1)}_{\nu-1/2}(kR_1)H^{(2)}_{\nu\mp1/2}(kR_2) \pm H^{(1)}_{\nu+1/2}(kR_1)H^{(2)}_{\nu\pm1/2}(kR_2)\big]. \tag{14}$$

III. RESULTS AND DISCUSSION

The linear-response conductance is calculated according to the Landauer-Büttiker formula [14,15]

$$G = \frac{I}{V} = g_0\sum_{j=\pm1/2,\pm3/2,\ldots} T_j, \tag{15}$$

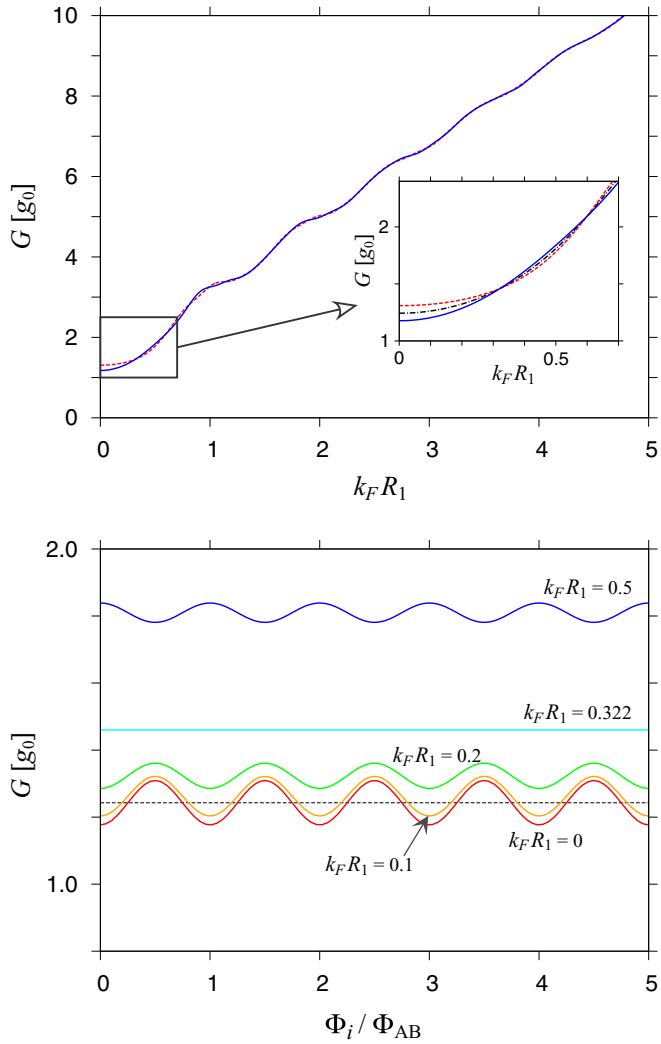

FIG. 2. Conductance as a function of the doping (top) and the flux piercing the inner disk area (bottom) for the radii ratio $R_2/R_1 = 5$. (Top) Different lines correspond to $\Phi_i = 0$ (blue solid line) and $\Phi_i = \Phi_{AB}/2$ (red dashed line). Inset presents a zoom-in, for low dopings, with an additional black dash-dot line depicting the conductance averaged over Φ_i. (Bottom) The doping is varied from $k_F R_1 = 0$ to $k_F R_1 = 0.5$ and specified for each solid line on the plot. Dashed line marks the pseudodiffusive conductance $G_{\rm diff} = 2g_0/\ln(R_2/R_1)$, with $g_0 = 4e^2/h$.

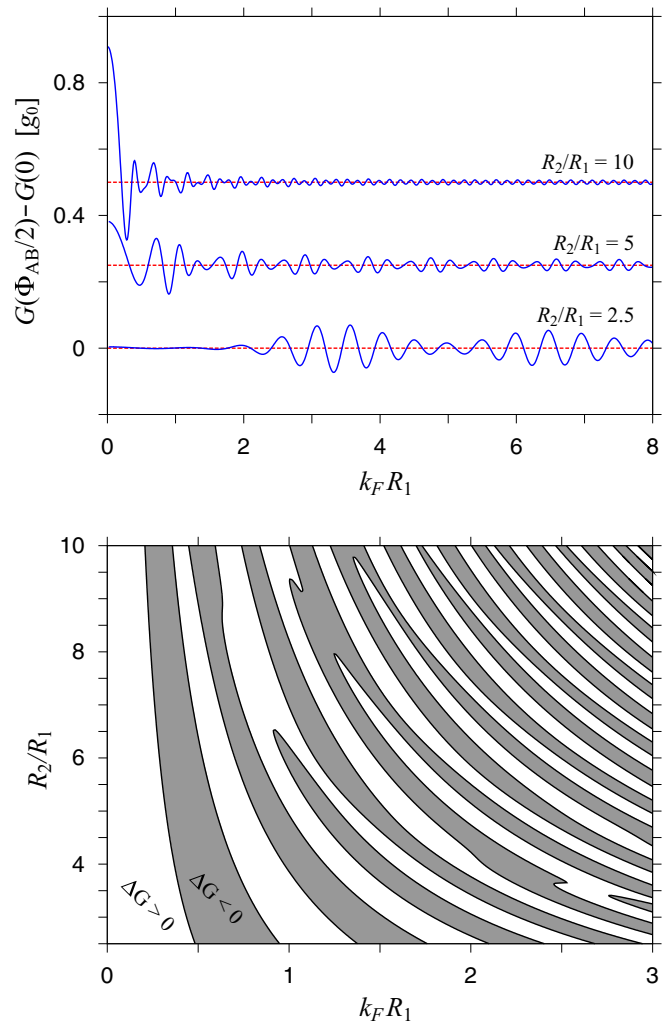

FIG. 3. (Top) Magnitude of the conductance oscillations, $\Delta G = G(\Phi_{AB}/2) - G(0)$, displayed as a function of the doping for selected values of the radii ratio (specified for each line). Notice that the data sets for $R_2/R_1 = 5$ and 10 (blue solid lines) are subjected to vertical shifts of 0.25 and $0.5g_0$ (respectively). Red dashed line shows the actual $\Delta G = 0$ for each case. (Bottom) Nodal lines (black solid) of ΔG as a function of the doping and the radii ratio, separating the areas with $\Delta G > 0$ (white) and $\Delta G < 0$ (shadow).

where the conductance quantum $g_0 = 4e^2/h$, with the factor 4 accounting for spin and valley degeneracy, and the summation over modes is performed numerically up to the machine round-off errors [27]. Our numerical results are presented in Figs. 2 and 3.

The asymptotic properties of the Hankel functions [28] in Eq. (13) lead to $T_j \approx 1$ for $k_F R_1 - \nu(j) \gg 1$, with $\nu(j)$ given by Eq. (9), or to $T_j \approx 0$ for $\nu(j) - k_F R_1 \gg 1$. In turn, the conductivity can by approximated as $G \approx 2g_0 k_F R_1$ for $k_F R_1 \gg 1$ and $R_2 \gg R_1$ (see top panel in Fig. 2), with an excess value of $\sim g_0 R_1/R_2$ (up to the order of magnitude) representing the contribution from evanescent waves.

Furthermore, the structure of Eqs. (9), (13), (14), and (15) results in perfectly periodic functional dependence of $G(\Phi)$, with a period Φ_{AB}, at arbitrary doping (see Fig. 2). Quite surprisingly, the magnitude of the conductance oscillations

$$\Delta G = G(\Phi_{AB}/2) - G(0), \tag{16}$$

takes relatively large absolute values (namely, $|\Delta G| > 0.1\, g_0$) not only in small vicinity of the charge neutrality-point, but also at higher dopings (see Fig. 3), signaling the importance of transport via evanescent waves again. [Notice that the difference between $G(\Phi_{AB}/2)$ and $G(0)$, defining ΔG via Eq. (16), is governed by only a few modes for which $k_F R_1 \approx \nu(j)$ and thus T_j's are neither ≈ 0 nor ≈ 1.] A systematic growth of ΔG with R_2/R_1 is visible for $k_F \to 0$ (with $\Delta G \approx g_0$ for $R_2 \gg R_1$), in consistency with earlier predictions of Refs. [2,3] for the uniform magnetic field case.

For each radii ratio, one can find a unique series of discrete doping values for which $\Delta G = 0$, resulting in $G(\Phi_i) = \text{const}$.

For instance, if $R_2/R_2 = 5$, the first five nodes of ΔG correspond to

$$(k_F R_1)_{\Delta G=0} = 0.322,\ 0.598,\ 0.814,\ 0.987,\ 1.137. \quad (17)$$

Below the first nodal value (i.e., $|k_F R_1| < 0.322$), we have $\Delta G > 0$ [or, equivalently, $G(\Phi_{\rm AB}) > G(0)$, see Eq. (16)]; then, the sign of ΔG alternates with growing $k_F R_1$, as indicated in the bottom panel in Fig. 3.

It is also visible in Fig. 3 that the pattern of nodal lines is rather irregular, as one could expect since ΔG can be regarded as the rational expression containing Bessel function. Typical separation between the first nodes of ΔG in Eq. (17) can (roughly) be approximated as $\Delta k_F R_1 \approx 0.3$, which corresponds, for the physical size of $R_1 = 50$ nm, to the energy interval of $\Delta E_F/k_B \approx 40$K (with the Boltzmann constant k_B). In turn, the conductance oscillations should be observable in comparable or higher temperatures then the standard Aharonov-Bohm effect in graphene rings [29,30].

IV. CONDUCTANCE OSCILLATIONS IN THE ABSENCE OF CYLINDRICAL SYMMETRY

So far, the discussion was limited to the case of a perfect cylindrical symmetry, allowing us to calculate the transmission probabilities T_j [see Eq. (13)] analytically by solving the scattering problem separately for each (jth) angular-momentum mode. In real system, several factors may break the cylindrical symmetry, resulting in the mode mixing. In particular, both the spatial corrugations of a graphene sheet and charge-donating impurities placed in the substrate lead to the charge density fluctuations (i.e., *p-n puddles*) [16,31–33]. For best existing devices, carrier density fluctuations are $\delta n < 10^{11}$ cm^2 near the neutrality point, corresponding to the electrostatic potential fluctuation of the order of $\delta U \sim 10$ meV.

Here we test numerically, how robust the effects described in Sec. III are against the cylindrical symmetry breaking. For this purpose, the electrostatic potential energy in the Hamiltonian (4) is replaced by [7]

$$U(r,\varphi) = -\frac{U_0 r}{R_2}\sin\varphi, \qquad R_1 < r < R_2. \quad (18)$$

In the leads, $r < R_1$ or $r > R_2$, we set $U(r,\varphi) = U_\infty$ again. The potential amplitude (without loss of generality, we suppose $U_0 \geqslant 0$) defines the Fermi energy range, $-U_0 < E_F < U_0$, for which a p-n interface is present in the disk area (see Fig. 4). A special case of $U_0 = 0$ restores the uniform-doping case considered in Sec. III.

Regardless of the value of U_0, angular-momentum eigenfunctions of the form given by Eqs. (6), (11), and (12), still represent the correct solutions in the leads. Therefore the numerical mode matching can be performed in the angular-momentum space, employing the transfer matrix approach presented with details in Ref. [7]. Since the Fermi wave number $k_F = |E_F - U(r,\varphi)|/(\hbar v_F)$ is now position-dependent, the numerical results presented in Fig. 4 are parametrized by E_F and U_0. In order to specify these quantities in the physical units, we fixed the disk dimensions at $R_1 = 50$ nm and $R_2 = 5R_1 = 250$ nm [34]. However, it is worth to stress

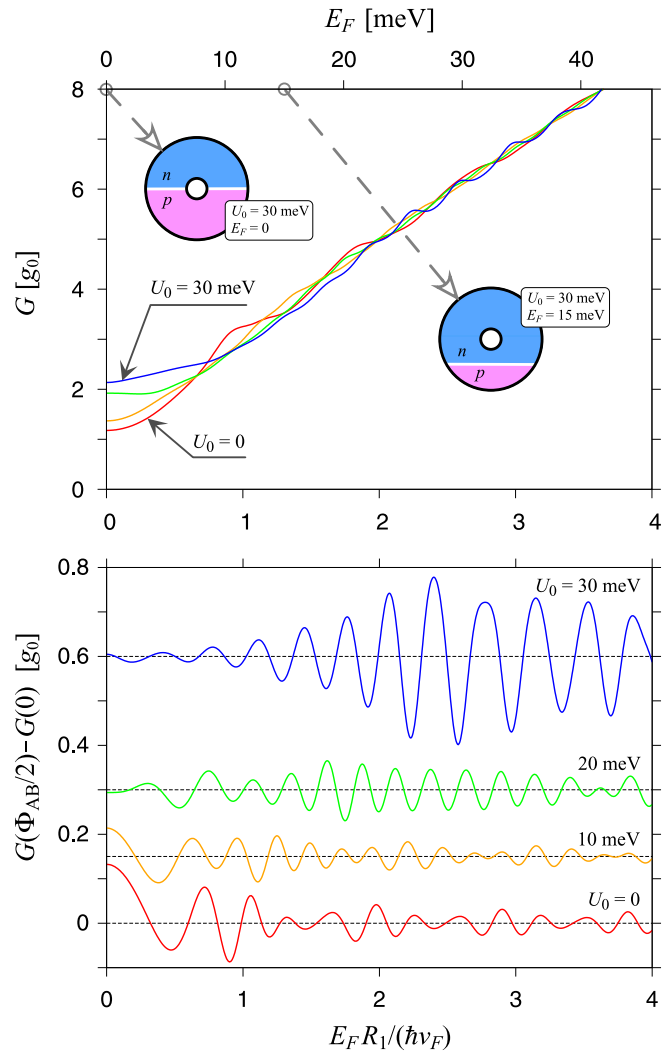

FIG. 4. Conductance for $\Phi_i = 0$ (top) and the oscillation magnitude (bottom) displayed as functions of the Fermi energy for the disk radii $R_1 = R_2/5 = 50$ nm and the electrostatic potential amplitude [see Eq. (18)] varied from $U_0 = 0$ to 30 meV with the steps of 10 meV. Top: Two insets show the positions of a *p-n* interface in the disk area for $U_0 = 20$ meV and the two different values of E_F. (Bottom) The data sets for $U_0 > 0$ (solid lines) are subjected to vertical shifts; black dashed lines show the actual $\Delta G = 0$.

that the transport characteristics are determined by the dimensionless parameters, $E_F R_1/(\hbar v_F)$ (also displayed in Fig. 4), $U_0 R_1/(\hbar v_F)$, and the radii ratio R_2/R_1, and therefore remain invariant upon the scaling $R_{1(2)} \to \lambda R_{1(2)}$, $E_F \to E_F/\lambda$, and $U_0 \to U_0/\lambda$, with a real $\lambda > 0$.

If the system is close to the charge-neutrality point, namely for $|E_F| < U_0 R_1/R_2$, the conductance is noticeably enhanced with growing U_0 (see top panel in Fig. 4), as the propagation through heavily p-doped and n-doped areas supplements the transport via evanescent waves. (We further notice that the largest considered $U_0 = 30$ meV corresponds to $U_0 R_1/(\hbar v_F) \approx 2.6 \lesssim R_2/R_1$, and thus the system, at zero field, can be regarded as being in the crossover range between the pseudodiffusive and the ballistic charge transport regimes [35].) For higher $|E_F|$, the effect of U_0 becomes negligible,

and $G \approx 2g_0\langle k_F\rangle R_1$ with $\langle k_F\rangle = |E_F|/(\hbar v_F)$ being the average Fermi wavenumber on the inner disk edge ($r = R_1$).

The magnetoconductance oscillations magnitude (see bottom panel in Fig. 4) are diminished for $|E_F| < U_0R_1/R_2$ with growing U_0. This observation can be rationalized by taking into account that at zero magnetic field main currents flow along the $\varphi \approx \pm\pi/2$ directions (i.e., towards the regions of extreme doping), for which the magnetic phases associated with the vector potential given by Eq. (5) vanish. In contrast, for the unipolar doping ($|E_F| > U_0$) the oscillations are only weakly affected by growing U_0, and the magnitudes of $\Delta G > 0.1\, g_0$ appear for wide range of the doping.

V. CONCLUSIONS

We have demonstrated, performing the numerical analysis of the exact formula for transmission probability for electron with a given angular momentum tunneling through the Corbino disk in graphene, that the conductance (as a function of magnetic flux piercing the disk) shows periodic oscillations of the Aharonov-Bohm kind. Unlike for a uniform magnetic field considered in Refs. [2,3], when similar oscillations appear at discrete Landau levels only, the disk in a solenoid magnetic potential shows the oscillations for any Fermi energy except from a discrete energy set, defined by the disk radii (R_1 and R_2), the Fermi velocity in graphene (v_F) and the Planck constant ($\hbar$), for which the conductance is flux-independent.

Most remarkably, away from the charge-neutrality point the conductance oscillations may show a significant magnitude ($\Delta G > 0.1\, g_0$, with $g_0 = 4e^2/h$) starting from moderate radii ratios $R_2/R_1 \gtrsim 2$, being comparable to the actual experimental values, see Refs. [9,10]. At the charge neutrality point, the oscillation magnitude grows with the radii ratio, approaching $\Delta G \approx g_0$ for $R_2 \gg R_1$.

Also, we find out that the conductance oscillations are well-pronounced in the presence of a position-dependent electrostatic potential that breaks the cylindrical symmetry and introduces the mode mixing. Some suppression of the effect is predicted for ambipolar dopings (i.e., with a *p-n* junction in the disk area), but the oscillations are restored away from the charge neutrality point (for unipolar dopings).

ACKNOWLEDGMENTS

We thank Piotr Witkowski for discussions. The work was supported by the National Science Centre of Poland (NCN) via Grant No. 2014/14/E/ST3/00256.

[1] A. Rycerz, P. Recher, and M. Wimmer, Phys. Rev. B **80**, 125417 (2009).
[2] A. Rycerz, Phys. Rev. B **81**, 121404(R) (2010).
[3] M. I. Katsnelson, Europhys. Lett. **89**, 17001 (2010).
[4] Z. Khatibi, H. Rostami, and R. Asgari, Phys. Rev. B **88**, 195426 (2013).
[5] B. Abdollahipour and E. Moomivand, Physica E **86**, 204 (2017).
[6] G. W. Jones, D. A. Bahamon, A. H. Castro Neto, and V. M. Pereira, Nano Lett. **17**, 5304 (2017).
[7] D. Suszalski, G. Rut, and A. Rycerz, J. Phys. Mater. **3**, 015006 (2020).
[8] J. Yan and M. S. Fuhrer, Nano Lett. **10**, 4521 (2010).
[9] E. C. Peters, A. J. M. Giesbers, M. Burghard, and K. Kern, Appl. Phys. Lett. **104**, 203109 (2014).
[10] M. Kumar, A. Laitinen, and P. Hakonen, Nat. Commun. **9**, 2776 (2018).
[11] Y. Zeng, J. I. A. Li, S. A. Dietrich, O. M. Ghosh, K. Watanabe, T. Taniguchi, J. Hone, and C. R. Dean, Phys. Rev. Lett. **122**, 137701 (2019).
[12] C.-I. Liu, D. S. Scaletta, D. K. Patel, M. Kruskopf, A. Levy, H. M. Hill, and A. F. Rigosi, J. Phys. D: Appl. Phys. **53**, 275301 (2020).
[13] M. I. Katsnelson, *Graphene: Carbon in Two Dimensions* (Cambridge University Press, Cambridge, 2012), Chap. 3.
[14] R. Landauer, IBM J. Res. Dev. **1**, 223 (1957).
[15] M. Büttiker, Y. Imry, R. Landauer, and S. Pinhas, Phys. Rev. B **31**, 6207 (1985).
[16] C. R. Dean, A. F. Young, I. Meric, C. Lee, L. Wang, S. Sorgenfrei, K. Watanabe, T. Taniguchi, P. Kim, K. L. Shepard *et al.*, Nat. Nanotechnol. **5**, 722 (2010).
[17] G. Rut and A. Rycerz, Philos. Mag. **95**, 599 (2015).
[18] D. A. Siegel, C.-H. Park, C. Hwang, J. Deslippe, A. V. Fedorov, S. G. Louie, and A. Lanzara, Proc. Natl. Acad. Sci. USA **108**, 11365 (2011).
[19] C. Hwang, D. A. Siegel, S.-K. Mo, W. Regan, A. Ismach, Y. Zhang, A. Zettl, and A. Lanzara, Sci. Rep. **2**, 590 (2012).
[20] L. M. Martelo, M. Dzierzawa, L. Siffert, and D. Baeriswyl, Z. Phys. B **103**, 335 (1997).
[21] J. D. Stokes, H. P. Dahal, A. V. Balatsky, and K. S. Bedell, Philos. Mag. Lett. **93**, 672 (2013).
[22] D. A. Abanin, I. Skachko, X. Du, E. Y. Andrei, and L. S. Levitov, Phys. Rev. B **81**, 115410 (2010).
[23] D. S. Lee, V. Skákalová, R. T. Weitz, K. von Klitzing, and J. H. Smet, Phys. Rev. Lett. **109**, 056602 (2012).
[24] More generally, for a centrosymmetric field $\mathbf{B} = B(r)\hat{e}_z$, the fraction $\phi = \Phi_d/\Phi_0$ in Eq. (1) is replaced by

$$\phi \equiv \frac{\Phi_i}{\Phi_{\rm AB}} + \frac{4\pi}{\Phi_0}\int_{R_1}^{R_2}\frac{dr}{r}\int_{R_1}^{r} dr' r' B(r),$$

where Φ_i is flux through the inner ring ($r < R_1$). In particular, if $B(r) = 0$ for $r > R_1$, the Aharonov-Bohm-like oscillations occur when varying Φ_i.
[25] Yu.V. Nazarov and Ya. M. Blanter, *Quantum Transport: Introduction to Nanoscience* (Cambridge University Press, Cambridge, UK, 2009), Chap.1.
[26] R. P. Feynman, R. B. Leighton, and M. L. Sands, *The Feynman Lectures on Physics* (Addison-Wesley, Reading, MA, 1963), Vol. II, Chap. 14.

[27] We calculated the Hankel functions, $H_\nu(x)^{(1,2)} = J_\nu(x) \pm iY_\nu(x)$ with $\nu \geqslant 0$, employing the double-precision regular [irregular] Bessel function of the fractional order $J_\nu(x)$ [$Y_\nu(x)$] as implemented in Gnu Scientific Library (GSL), see https://www.gnu.org/software/gsl/doc/html/specfunc.html bessel-functions. For $\nu < 0$, we use $H^{(1)}_{-\nu}(x) = e^{i\pi\nu}H^{(1)}_\nu(x)$ or $H^{(2)}_{-\nu}(x) = e^{-i\pi\nu}H^{(2)}_\nu(x)$.

[28] G. Nemes, Acta Appl. Math. **150**, 141 (2017).

[29] S. Russo, J. B. Oostinga, D. Wehenkel, H. B. Heersche, S. S. Sobhani, L. M. K. Vandersypen, and A. F. Morpurgo, Phys. Rev. B **77**, 085413 (2008).

[30] C. Stampfer, E. Schurtenberger, F. Molitor, J. Guettinger, T. Ihn, and K. Ensslin, Int. J. Mod. Phys. **23**, 2647 (2009).

[31] Y. Zhang, V. W. Brar, C. Girit, A. Zettl, and M. F. Crommie, Nat. Phys. **5**, 722 (2009).

[32] S. Samaddar, I. Yudhistira, S. Adam, H. Courtois, and C. B. Winkelmann, Phys. Rev. Lett. **116**, 126804 (2016).

[33] A. Jayaraman, K. Hsieh, B. Ghawri, P. S. Mahapatra, and A. Ghosh, arXiv:2003.02880.

[34] We took the nearest-neighbor hopping integral in graphene $t = 2.7$ eV and the lattice parameter $a = 0.246$ nm, leading to $\hbar v_F = \sqrt{3}ta/2 = 0.575$ eV nm.

[35] For $E_F = 0$, the parameter $u_0 = U_0R_1^2/(R_2\hbar v_F)$ allows one to distinguish between the pseudodiffusive ($u_0 \ll 1$) and the ballistic ($u_0 \gg 1$) charge transport regimes, with crossover occurring for $u_0 \sim 1$; see also Ref. [7].